

Ensemble Modeling of CME Propagation

C.O. Lee · C.N. Arge · D. Odstrčil · G. Millward ·
V. Pizzo · J.M. Quinn · C.J. Henney

Received: 31 January 2012 / Accepted: 17 March 2012 / Published online: 17 April 2012
© Springer Science+Business Media B.V. 2012

Abstract The current progression toward solar maximum provides a unique opportunity to use multi-perspective spacecraft observations together with numerical models to better understand the evolution and propagation of coronal mass ejections (CMEs). Of interest to both the scientific and forecasting communities are the Earth-directed “halo” CMEs, since they typically produce the most geoeffective events. However, determining the actual initial geometries of halo CMEs is a challenge due to the plane-of-sky projection effects. Thus the recent 15 February 2011 halo CME event has been selected for this study. During this event the *Solar Terrestrial Relations Observatory* (STEREO) A and B spacecraft were fortuitously located $\sim 90^\circ$ away from the Sun–Earth line such that the CME was viewed as a limb event from these two spacecraft, thereby providing a more reliable constraint on the initial CME geometry. These multi-perspective observations were utilized to provide a simple geometrical description that assumes a cone shape for a CME to calculate its angular width and central position. The event was simulated using the coupled Wang–Sheeley–Arge (WSA)-Enlil 3D numerical solar corona-solar wind model. Daily updated global photospheric magnetic field maps were used to drive the background solar wind. To improve our modeling techniques, the sensitivity of the modeled CME arrival times to the initial input CME geometry was assessed by creating an ensemble of numerical simulations based on multiple sets of cone parameters for this event. It was found that the accuracy of the modeled arrival times not only depends on the initial input CME geometry, but also on the accuracy of the modeled solar wind background, which is driven by the input maps of the photospheric field. To improve the modeling of the background solar wind, the recently

Observations and Modelling of the Inner Heliosphere
Guest Editors: Mario M. Bisi, Richard A. Harrison, Noé Lugaz

C.O. Lee (✉) · C.N. Arge · J.M. Quinn · C.J. Henney
Air Force Research Laboratory/Space Vehicles Directorate, Kirtland Air Force Base, NM, USA
e-mail: cleevantilborg@gmail.com

D. Odstrčil
George Mason University, Fairfax, VA, USA

G. Millward · V. Pizzo
NOAA Space Weather Prediction Center, Boulder, CO, USA

developed data-assimilated magnetic field synoptic maps produced by the Air Force Data Assimilative Photospheric flux Transport (ADAPT) model were used. The ADAPT maps provide a more instantaneous snapshot of the global photospheric field distribution than that provided by traditional daily updated synoptic maps. Using ADAPT to drive the background solar wind, an ensemble set of eight different CME arrival times was generated, where the spread in the predictions was ~ 13 hours and was nearly centered on the observed CME shock arrival time.

Keywords Coronal mass ejections, modeling · Solar wind, modeling · Solar wind, observations

1. Introduction

The forecasting of the ambient solar wind has become increasingly successful throughout the years. A number of physics-based solar corona–solar wind models use routine magnetic field observations of the solar photosphere as input boundary conditions to drive numerical simulations (*e.g.*, Arge *et al.*, 2004; Riley, Linker, and Mikic, 2001; Odstrcil *et al.*, 2002; Mikić and Linker, 1995; Cohen *et al.*, 2008). The success of these models in accurately modeling the solar wind structures has resulted in their use for routine space weather predictions by the National Oceans and Atmospheric Administration (NOAA) Space Weather Prediction Center (SWPC; Pizzo *et al.*, 2011) and as scientific research tools through the runs-on-request service at the Community Coordinate Modeling Center (CCMC; <http://ccmc.gsfc.nasa.gov>).

During magnetically active solar conditions, the space environment is far less predictable. Solar transients called coronal mass ejections (CMEs) travel through interplanetary space and disturb the ambient solar wind structure. Until recently, knowledge of the interplanetary counterparts of CMEs (ICMEs) have been limited to ground- and space-based observations as well as *in situ* spacecraft measurements obtained at L1 (~ 1.5 million km upstream of Earth, along the Sun–Earth line). For a recent in-depth review on the origin, evolution, and propagation effects of ICMEs, see Forsyth *et al.* (2006).

Such dramatic changes in the solar wind conditions caused by the passage of an ICME can trigger strong geomagnetic storms that impact our society’s technological systems one to four days later. One of the most notable geomagnetic storms caused by CMEs occurred during the previous solar maximum. The 2003 “Halloween Storms” produced substantial changes in the solar wind conditions that created damaging effects on our technological systems. Many satellites around Earth experienced power failure while others went into safe mode or experienced saturation with on board sensors (Webb and Allen, 2004). At the ground level, technological systems were also affected in locations such as Wisconsin and New York, where increased current levels were detected in transmission lines (Webb and Allen, 2004).

The harmful effects of such events on our technology can be mitigated through advanced warnings of CMEs and their subsequent impacts on our geospace environment, given the progress that has been made in developing more robust solar wind codes that can capture the global CME properties and predict reliable CME arrival times. Recently, NOAA/SWPC transitioned into operations a Sun-to-Earth solar wind model, the Wang–Sheeley–Arge (WSA) corona model (Arge and Pizzo, 2000; Arge *et al.*, 2003, 2004) coupled with the Enlil solar wind model (Odstrcil, 2003), for routine space weather predictions (Pizzo *et al.*, 2011). To model a CME event using WSA–Enlil, one of the methods that is

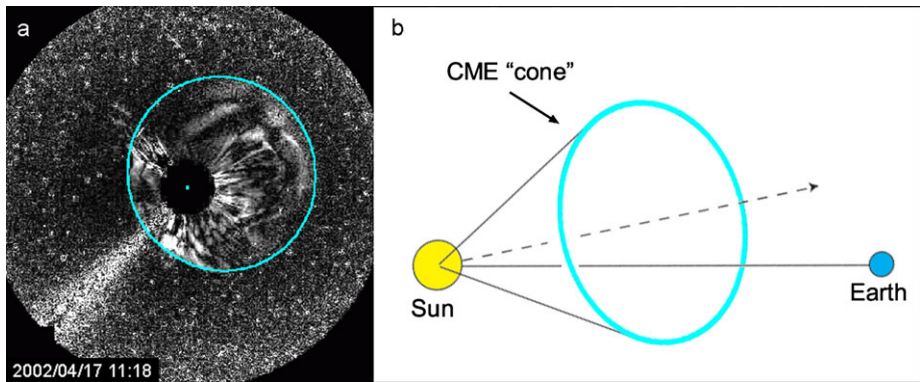


Figure 1 (Left) Example of a cone-ellipse superposed on a differenced white light CME image from the LASCO instrument on board the SOHO spacecraft. (Right) Illustration of cone orientation and angular width for an Earth-directed (halo) CME.

used by NOAA/SWPC is an iterative graphical tool that uses a cone shape for a CME (Figure 1) to estimate its initial radial speed, size, and propagation direction. Based on these parameters, a cone-shaped CME is injected into the WSA-Enlil numerical grid for simulation of its evolution and propagation to the orbit of Earth at one astronomical unit (AU, ~ 150 million km).

Although several techniques are available for characterizing a CME (e.g., see Davis *et al.*, 2011; Möstl *et al.*, 2011; Lugaz, 2010; Byrne *et al.*, 2010; Liu *et al.*, 2010; and references therein), the advantage of using the cone formulation to calculate the geometrical and kinematic properties of a CME is that the fitting tool is easy and fast to use, which is ideal for real-time space weather forecasting. The cone formulation offers a good approximation for describing the geometry and kinematics of a CME that is propagating toward an observer.

As the next solar maximum period approaches, the WSA-Enlil-cone modeling system will be used as a routine forecasting tool for geomagnetic storm predictions in addition to its current use as a research tool to study CME evolution and propagation. Thus, we provide in this study an example of how to assess the sensitivity of the WSA-Enlil-cone results, such as the CME arrival times, to the initial input cone-shaped CME geometry. In practice, a single set of cone parameters is generated for a CME event, whereby a user of the cone tool manually fits an ellipse over a white light coronagraph image of a CME (Figure 1). Because variations in the cone parameters will naturally occur for each person making a fit to the same CME due to ambiguities in identifying the ejecta structure, it is useful to quantify how much the predicted arrival time values and other modeling parameters are influenced by the manual fitting process. We thus make multiple, yet slightly different cone model fits to generate an ensemble of fits so that we obtain a set of varying predictions that can reveal the uncertainties in a model forecast of a CME arrival time. The details of how we vary the cone fits will be described here. Our assessment will help current and future users of the WSA-Enlil-cone modeling system interpret and understand the simulation results (e.g., at the NOAA/SWPC operations page or at the CCMC runs-on-request site) and will also provide feedback to the model developers for ongoing improvements to the system.

For this ensemble study, the Earth-directed “halo” CME event that occurred on 15 February 2011 is selected. During this time, the twin *Solar Terrestrial Relations Observatory* (STEREO; Kaiser, 2005) A and B spacecraft, which have been traveling ahead and behind Earth along its orbit, were positioned $\sim 90^\circ$ away from the Sun–Earth line (Figure 2a) such

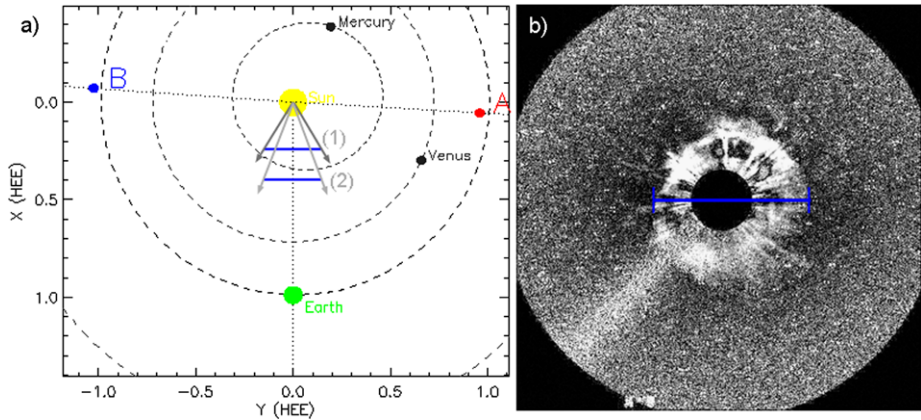


Figure 2 (a) Ecliptic view of the inner heliosphere. Shown is the orientation of the STEREO A and B spacecraft with respect to Earth on 15 February 2011. STEREO A was located at $\sim 87.1^\circ$ west, with respect to the Sun–Earth line, whereas STEREO B was located at $\sim 93.7^\circ$ east. (b) Differenced SOHO/LASCO C3 coronagraph image of the CME. The blue horizontal line shows the width across the bright outermost ejecta features, also shown in panel (a). As discussed in Section 2, the radial distance of the leading front and the angular width of the CME are ambiguous when viewed along the line of sight; that is, it is unclear if we are observing a slower CME that is wide (situation 1 in panel (a)) or a faster CME that is narrow (situation 2 in panel (a)). Image credit: NASA STEREO Science Center and SOHO/LASCO.

that the event was observed near the solar limb by both spacecraft. Such limb observations help to constrain the initial CME characteristics during the fitting process.

In Section 2 we describe our approach in using a version of the geometrical cone tool developed by NOAA/SWPC together with white light coronagraph images at L1 to obtain our ensemble of cone parameters for the 15 February 2011 CME event. We also discuss how the STEREO white light observations are used to better constrain our cone parameters. In Section 3 we discuss the WSA-Enlil modeling system and the input synoptic maps that are used to drive the background solar wind. Here we also present our ensemble simulation results. It is shown that the accuracy of the modeled arrival times depends not only on the initial input CME geometry determined from the cone tool, but also upon the initial accuracy of the modeled solar wind background, as driven by the input solar magnetograms. In Section 4 we present another set of simulation results that were driven with the recently developed data-assimilated synoptic maps produced by the Air Force Data Assimilative Photospheric flux Transport (ADAPT) model (Arge *et al.*, 2010, 2011; Henney *et al.*, 2012). These maps provide a more instantaneous snapshot of the global photospheric field distribution. In Section 5, we assess and discuss the sensitivity of the predicted arrival times to the small variations in the cone fitting parameters. A summary of our results with concluding remarks is presented in Section 6.

2. Ensemble Cone Parameters

In this study we use the cone software routine developed at NOAA/SWPC. The use of a cone shape (Figure 1) to describe a CME is ideal since CMEs commonly expand radially outward, to first order, in a self-similar way (see Zhao, Plunkett, and Liu, 2002 and references therein). The cone routine uses the mathematical approach of fitting cones described in Xie, Ofman, and Lawrence (2004), which is based on an earlier study by Zhao, Plunkett, and Liu (2002).

The underlying assumptions of the cone formulation are: i) beyond the solar corona the angular width of the CME is more or less constant (*e.g.*, Webb *et al.*, 1997 presents such observational evidence), ii) the CME propagation direction and speed are essentially radial, iii) the source location of the halo CME is near the center of the solar disk and the area of the active region, and iv) the expansion of the CME is isotropic.

2.1. Constraining Cone Fits Using STEREO

To make cone fits, white light coronagraph images of a CME event are read into the NOAA/SWPC cone routine. These images are obtained at L1 by the *Solar and Heliospheric Observatory* (SOHO) *Large Angle and Spectrometric CO*ronagraph (LASCO; Brueckner *et al.*, 1995) C3 coronagraph, which has a field of view (FOV) of $3.8 R_{\odot}$ to $32 R_{\odot}$. A time sequence of LASCO images is selected such that the CME features are bright and appear consistently throughout the set. In addition, one LASCO image without the CME (the base image) is selected for differencing the set of CME observations (*e.g.*, Figure 2b). The brightness and the contrast of the differenced images can be adjusted to enhance the fainter halo CME features.

During the initial fitting over one LASCO image, two free cone parameters must be defined at the cone software graphical interface: the CME leading edge distance and the angular width. Ideally, these parameters would be estimated directly from the LASCO CME image. Because these observations are obtained along the line of sight, to simultaneously estimate the leading edge distance and the angular width is a challenge, since their values are not unique from this vantage point. For example, in Figure 2b, it is not possible to distinguish whether we see a bright halo front that is wide in angle at a lesser heliocentric distance (situation 1 in Figure 2a), or a bright front that is narrow at a larger heliocentric distance (situation 2 in Figure 2a). For a given launch time, it is implied in situation 2 that the CME is propagating away from the Sun at a faster radial speed than the CME in situation 1.

For non-limb CMEs, *i.e.*, those with a propagation component in the direction toward Earth, previous studies have shown that the plane-of-sky projection effects alter the observed CME properties such that: i) the apparent angular width is greater than the true angular width, and ii) the apparent leading edge distance from the Sun is less than the true leading edge distance (Burkepile *et al.*, 2004; Hundhausen, Burkepile, and Cyr, 1994; and references therein). The implication for space weather forecasting lies in the accuracy of the predicted CME arrival time at 1 AU: if the apparent leading edge distance is estimated to be less (greater) than the true distance, the predicted arrival time of the CME will be later (earlier) than the actual arrival time. Overall, the influence of the projection effects is greatest when the central axis of the CME is orthogonal to the plane of the sky (*i.e.*, coaligned with the observer's line of sight), as is the case when a halo CME event occurs.

To produce the cone fits more rigorously, limb observations of the 15 February 2011 CME event from the STEREO B *Sun Earth Connection Coronal and Heliospheric Investigation* (SECCHI) COR2 coronagraph (<http://secchi.nrl.navy.mil/>) are used to better constrain the angular width and the leading edge distance. Note that the STEREO/COR2 observations have a FOV of $2.5 R_{\odot}$ to $15 R_{\odot}$, which overlaps with the LASCO C3 observations. From the STEREO observation at $\sim 04:08$ UT (Figure 3b, described in the next section) we measured values of $\sim 11.5 R_{\odot}$ to $\sim 12.5 R_{\odot}$ and $\sim 65^{\circ}$ to $\sim 85^{\circ}$ for the CME leading edge distance and full angular width, respectively. The spread in the values is attributed to the CME features from which the measurements are made. For example, smaller angular widths are obtained if we measure from the bright CME “legs” (angle formed by the lighter

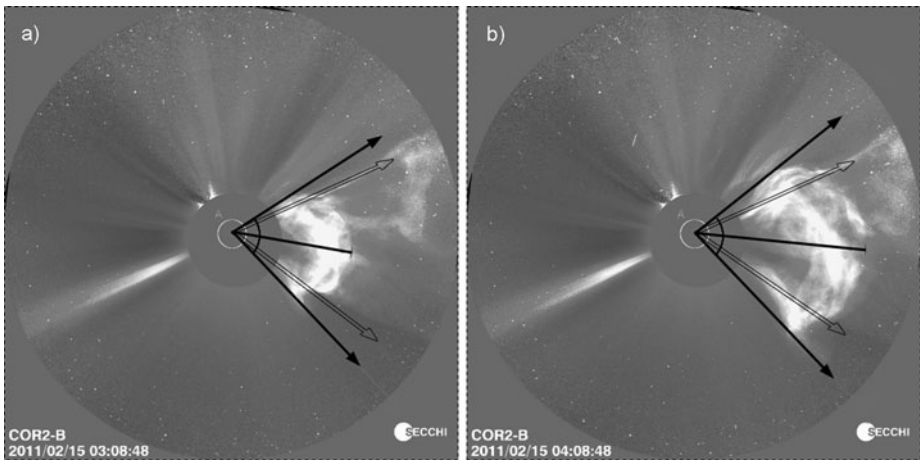


Figure 3 STEREO/SECCHI COR2-B white light coronagraph images of the 15 February 2011 CME. During this time STEREO B was trailing behind Earth at $\sim 90^\circ$ such that the Earth-directed CME was observed over the western solar limb from its vantage point (see Figure 2a). From these images we measure the angular width of the CME (pair of black arrow lines) as well as the radial distance of its bright front (black bisecting line).

arrows in Figure 3) than from the widest, bright features of the CME (angle formed by the black arrows in Figure 3). For the CME leading edge distance, the measurements were less ambiguous, since the CME front is better defined and thus the spread in the measured values is smaller. In general, the variation in our measured CME angular widths and leading edge distances from the STEREO limb observations reflects the subjectivity in making these measurements and likely represents the variations that would naturally occur when different individuals measure such parameters.

2.2. Making the Cone Fits

To obtain a consistent picture of the CME evolution, the STEREO images used in this study are those with snapshot times that coincided most closely with the LASCO observations used. Figure 4a shows the LASCO C3 “primary” image that is used for the initial fitting; it has a snapshot time of $\sim 04:06$ UT, which most closely matches the STEREO snapshot time of $\sim 04:08$ UT in Figure 3b.

A cone ellipse is fitted by hand over the outermost bright features of the CME structure in the primary image using the NOAA/SWPC cone tool. The size of the ellipse is adjusted through the graphical interface of the cone routine, based on the user-specified values for the angular width and leading edge distance of the CME front. Using the range of STEREO values as a guide, we first adjust the ellipse size by setting the leading edge distance value and then make smaller adjustments to the fit by setting the value for the angular width. We use this approach because of the larger ambiguity in the STEREO limb measurements for the widths *versus* the leading edge values, which was discussed earlier at the end of Section 2.1. The final adjustments to the fitting of the ellipse are made through small (and sensible) modifications to the values of one or both parameters. Meanwhile, the position of the cone ellipse in the plane of the LASCO image, which determines the source location of the cone CME, is manually adjusted at the graphical user interface.

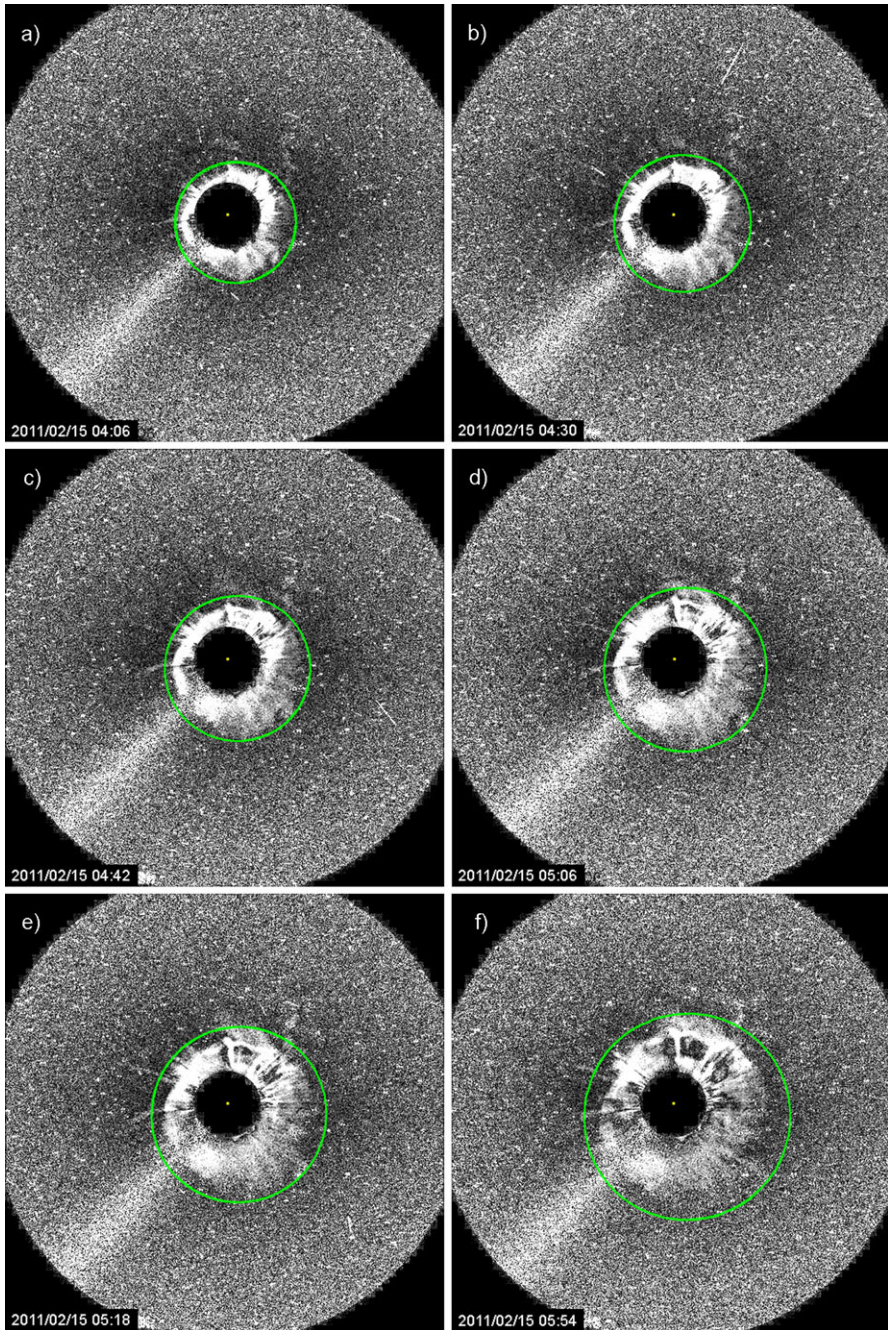


Figure 4 An example of a set of cone fits over the 15 February 2011 CME. The time sequence of base-differenced LASCO C3 white light coronagraph images shows the evolution of the CME (bright loop-like structure) as it propagates toward Earth. The field of view of each image is $3.8 R_{\odot}$ to $32 R_{\odot}$, with the black occulting disk at the center. The green ellipse shown in each image is our cone fit over the CME. In this example we obtained a full angular width of 68° and a radial velocity of 814 km s^{-1} at $21.5 R_{\odot}$. Image credit: SOHO/LASCO.

Once the initial fit to the primary image is finalized, the width of the cone ellipse is fixed during subsequent fits using a number of “secondary” images (Figures 4b through 4f). Figure 4 shows a set of cone fits that were made over a selection of LASCO images. In this example, the (full) cone angular width of 68° was used. This value was measured from the bright “legs” of the CME, as shown in the STEREO limb observation (Figure 3b), and produced the best fit of the ellipse around the CME as shown (Figure 4). With the cone angular width fixed, during the fittings to the additional differenced LASCO CME images the adjustments to the size of the cone ellipse are determined from the user-provided values for the leading edge distance. Recall from the beginning of Section 2.1 that the brightness and contrast in the differenced LASCO images can be adjusted to enhance the fainter CME features. To be consistent throughout the fitting process (*e.g.*, to try to make subsequent fits using the same ejecta features in the selection of LASCO images), if some ejecta features that were used during the initial fitting appear fainter in the set of remaining LASCO images (as the CME propagated away from the Sun), one adjusts the brightness and/or contrast in order to bring out these features.

Note that for the primary image from which the initial fit is made, in the NOAA/SWPC tool it is not necessary to select the first image in the sequence of LASCO observations. For example, we could have selected Figure 4c as the primary image instead of Figure 4a, and used Figures 4a through 4b and Figures 4d through 4f as the secondary images for making the subsequent fits. However, since during the initial fitting both the leading edge distance and the angular width are used to best fit the cone ellipse over the CME, in order to constrain the ellipse using the limb observations by STEREO, for the primary image we thus selected the LASCO image (*e.g.*, Figure 4a) that has the snapshot time that most closely matched that of the STEREO observation (*e.g.*, Figure 3b).

After the fits are finalized, the cone software uses a first-order equation of a line to calculate the radial CME speed based on the snapshot times of the images together with the associated leading edge distance values that are used during the fits. From this equation, the values are extrapolated by the tool for the CME radial speed and the time at which the leading edge front reaches the distance of $21.5 R_\odot$, the inner boundary of the Enlil numerical modeling domain. By the end of the fitting process, four cone parameters are determined: the source location of the cone axis (latitude, longitude), the half angular width, the time when the CME leading edge front crosses $21.5 R_\odot$, and the radial speed at $21.5 R_\odot$.

The fitting process is repeated seven times to generate an ensemble set of cone parameters. To make a new fit each time, the LASCO images are reloaded into the NOAA/SWPC cone tool to ensure that all the parameters are reset to the software default values. This includes the brightness and contrast settings. For each fit, slightly different values for the angular width and leading edge distance are used, where variations are guided by the values obtained from the STEREO observations (see Section 2.1). Specifically, for each new primary fit of the set, the angular width is varied by an increment of a few degrees from the value used in the previous fit, whereas the leading edge distance is varied by an increment of 0.5 to $1 R_\odot$. Also for each new fit, slightly different CME features are used to make the initial fit over the primary image. In total, eight fits are made as a start to assess the number of fits needed for obtaining a representative spread in the CME arrival times, based on the variations to the input cone parameters. In future ensemble studies of other CME events, the number of cone fits will be reduced to see whether a statistically meaningful ensemble of arrival time predictions can be obtained.

Table 1 lists our ensemble of cone parameters and the WSA-Enlil predicted arrival times; the latter will be discussed in Section 3. In particular, column four lists the (full) angular cone widths that were used in the ensemble, as discussed in Section 2.1, where the values range

Table 1 List of cone fit parameters for the 15 February 2011 CME from a total of eight fits for our ensemble set. The fit numbers correspond to the numbers shown in Figure 7 of our modeled results (discussed in Section 3). The second and third columns contain the cone axis latitude and longitude, respectively. The sixth column provides the approximate CME arrival time predicted from the WSA-Enlil-cone simulation; the times are rounded to the closest half hour. In the last column, we compare the predicted arrival times with the ACE-observed arrival time of $\sim 01:30$ UT on 18 February 2011 (as marked by the gray vertical line in Figure 7) and calculate the difference ($\Delta t = t_{\text{observed}} - t_{\text{predicted}}$).

Fit	Source location		Full cone width ($^{\circ}$)	V_R at $21.5 R_{\odot}$ (km s^{-1})	Predicted arrival time at 1 AU (UT)	Δt
	Lat ($^{\circ}$)	Lon ($^{\circ}$)				
1	-12	3	68	558	23:00 17 Feb.	+2.5
2	-13	5	72	613	20:00 17 Feb.	+5.5
3	-12	5	68	622	19:00 17 Feb.	+6.5
4	-13	6	66	681	16:00 17 Feb.	+9.5
5	-11	5	62	727	13:30 17 Feb.	+12.0
6	-11	6	68	764	12:00 17 Feb.	+13.5
7	-13	5	62	806	10:30 17 Feb.	+15.0
8	-12	5	68	814	10:00 17 Feb.	+15.5

from 62° to 72° . Although a range of $\sim 65^{\circ}$ to $\sim 85^{\circ}$ for the CME width was measured from the STEREO observations (Figure 3), smaller angles are used in the ensemble cone fits given the constraints on the ellipse sizes by the leading edge distance values. When attempts were made to use larger cone width values (e.g., 85°), the leading edge distance values necessary for maintaining the fits around the CME were unrealistically small; i.e., the CME front was too close to the Sun, based on the STEREO limb observations.

3. Event Modeling

To simulate the background solar wind, we use the latest versions of the WSA corona model (version 2.2.2) and the Enlil solar wind model (version 2.6c). Note that we are using the same version of the coupled WSA-Enlil model as NOAA/SWPC for their space weather operations.

The WSA model (Arge and Pizzo, 2000; Arge *et al.*, 2003, 2004) is a combined empirical and physics-based model of the corona and solar wind; it is an improved version of the original Wang and Sheeley model (Wang and Sheeley, 1992, 1995). As its input, the WSA uses ground-based line-of-sight observations of the photospheric magnetic field, in the form of synoptic maps. The code begins by re-gridding the input synoptic map, which is generally in sine-latitude format, to a uniform resolution (i.e., grid cells in units of square degrees) specified by the user. The total magnetic flux is calculated over the map, and any residual monopole moment is uniformly subtracted from the map to ensure that the magnetic field is divergence free. The corrected map (e.g., Figure 5, top panel) is then used in a magnetostatic potential field source surface (PFSS) model (Schatten, Wilcox, and Ness, 1969; Altschuler and Newkirk, 1969; Wang and Sheeley, 1992), which determines the coronal field out to $2.5 R_{\odot}$. The output of the PFSS model serves as input to the Schatten Current Sheet (SCS) model (Schatten, 1971), which provides a more realistic magnetic field topology of the upper corona. Only the innermost portion of the SCS solution is used, i.e., from $2.5 R_{\odot}$ to $21.5 R_{\odot}$.

An empirical velocity relationship (Arge *et al.*, 2003, 2004) is then used to assign solar wind speed at the outer coronal boundary. It is a function of two coronal parameters: the flux

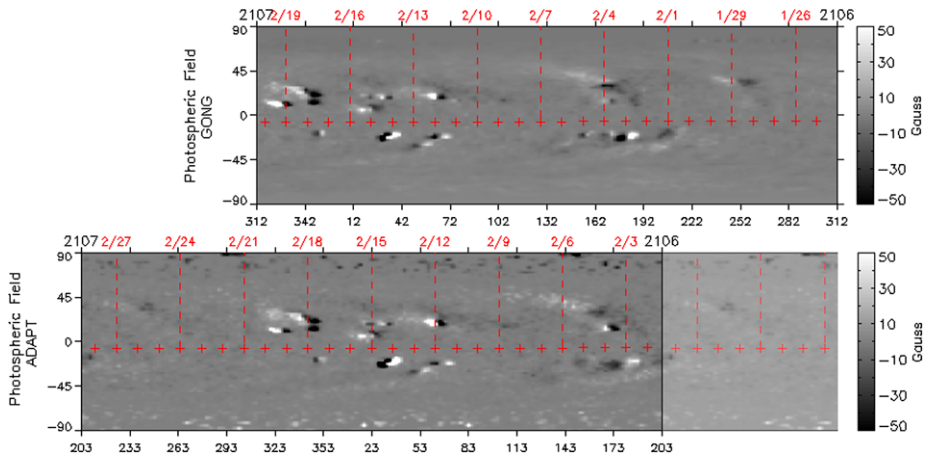


Figure 5 Synoptic maps of the photospheric radial magnetic field. The GONG daily updated map is shown (top) with a leading edge longitude of 312° of Carrington rotation 2107, which corresponds to 09:02 UT on 20 February 2011. The newest data are located on the left side of the map. The ADAPT-generated “daily updated” map is displayed (bottom) with a leading edge longitude of 203° of Carrington rotation 2107, which corresponds to 15:39 UT on 28 February 2011. In both panels, the + symbol labeled in red indicates the daily position of the sub-Earth point of the Sun, which varies between $\pm 7.25^\circ$ in solar latitude due to the inclination of the solar rotation axis with respect to the ecliptic plane. A comparison of the two panels is explained more fully in Section 4.

tube expansion factor (f_s) and the minimum angular separation at the photosphere between an open field footprint and the nearest coronal hole boundary. These parameters are determined by starting at the centers of each of the grid cells on the outer coronal boundary surface and tracing the magnetic field lines down to their footpoints rooted in the photosphere. The flux tube expansion factors are calculated using the traditional definition (Wang and Sheeley, 1992), $f_s = (R_{ph}/R_{ss})^2 (B_{ph}/B_{ss})$, where B_{ph} and B_{ss} are the field strengths along each flux tube at the photosphere ($R_{ph} = 1 R_\odot$) and at the source surface ($R_{ss} = 2.5 R_\odot$), respectively. The model provides the radial magnetic field and solar wind speed at the outer coronal boundary surface. The densities and temperatures, which are not provided by WSA, may be deduced by assuming mass flux conservation and pressure balance. When WSA is used to drive a magnetohydrodynamic (MHD) solar wind model, such as Enlil, the outer coronal boundary is typically set to a value beyond $\sim 15 R_\odot$ to ensure that the solar wind is supersonic and super-Alfvénic. For Enlil, this boundary is set to $21.5 R_\odot$.

The coronal parameters determined from the WSA model are used as the input boundary conditions for the Enlil solar wind model (Odstrcil, 2003). Enlil simulates the solar wind flow by calculating the solar wind velocity, density, temperature, magnetic field strength, and polarity throughout the inner heliosphere. For this study, a medium resolution spherical uniform mesh grid that consists of $320 \times 60 \times 180$ ($r \times \theta \times \phi$) grid points is used. The spacing between each grid point in the radial, latitudinal, and longitudinal directions is $0.67 R_\odot$, 2° , and 2° , respectively. To simulate a CME within Enlil, a pressure pulse is “injected” at the inner boundary of the numerical grid, where the cone-derived values for the speed, the source location, the angular width, and the time during which the CME front crosses $21.5 R_\odot$ are used to parameterize the ejecta.

Daily updated synoptic maps from the National Solar Observatory (NSO) *Global Oscillation Network Group* (GONG; Harvey *et al.*, 1996), which are obtained from <http://nso.gong.edu>, are used to drive the WSA model. We use the daily updated maps

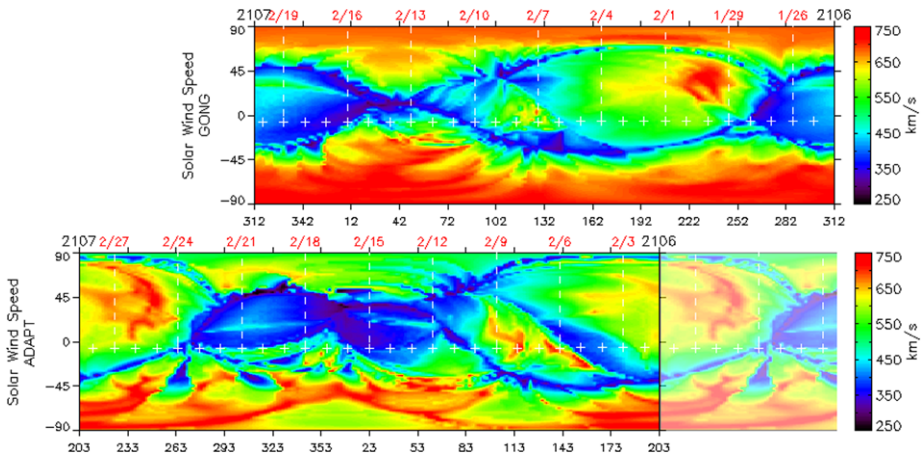


Figure 6 Same as for Figure 5 but for the WSA solar wind speeds at $21.5 R_{\odot}$. The solutions using the GONG daily updated map (top) and the ADAPT “daily updated” map (bottom) are shown. A comparison of the two panels is explained more fully in Section 4.

instead of the traditional full Carrington rotation maps because the daily updated maps consist of the most recent observations, particularly at the portion that is facing Earth and east of central meridian. For a good discussion on the advantages and disadvantages of using traditional *versus* daily updated synoptic maps, refer to Section 3 in Arge and Pizzo (2000). Figure 5 (top panel) shows the GONG daily updated map that is used as input for WSA. The calculated solar wind speeds at $21.5 R_{\odot}$ are shown in Figure 6 (top panel). To simulate the CME event, we ran each set of cone fits, as listed in Table 1, using the same WSA-Enlil background driven by the input map from GONG.

Figure 7 shows our ensemble simulation results (colored lines) for the solar wind radial speed, density, and the magnetic field magnitude at 1 AU. The results are compared with the *in situ*, near-ecliptic solar wind observations (black line) from the OMNI data set obtained from the NASA Goddard Space Flight Center Space Physics Data Facility (<http://spdf.gsfc.nasa.gov>). Specifically, we use the Level 2 hourly resolution data set. To determine the observed arrival time of the CME disturbance, we refer to the first steep rise in the solar wind speed and magnetic field (Figure 7, top and bottom panels, respectively). Taking the midway point between the onset time and the end of the steep rise (before the onset of the gradual rise), we deduce an arrival time (rounded to the closest half hour) of $\sim 01:30$ UT on 18 February 2011, as marked by the vertical gray line in Figure 7.

As seen in Figure 7, our ensemble results predict the CME to arrive too early compared to the actual arrival time (marked by the vertical gray line) when using the GONG daily updated map. The last two columns of Table 1 list the predicted arrival times, rounded to the closest half hour, based on our set of cone parameters as well as the difference between the predicted and observed arrival times, $\Delta t = t_{\text{observed}} - t_{\text{predicted}}$. In the table and the discussion here, + (−) Δt means that the predicted arrival time is too early (too late) compared to the observations. For the prediction that resides in the middle of our ensemble (hereafter called the “average” prediction), which is based on the cone parameters listed for fit number 4 in Table 1, the cone CME arrives at $\sim 16:00$ UT on 17 February 2011 (solid magenta time series in Figure 7), which is ~ 9.5 hours too early. Based on our earliest and latest predictions in our ensemble (blue and red times series in Figure 7), the spread in our ensemble of arrival times is ~ 13 hours, or $+6/-7$ hours about the middle “average” prediction.

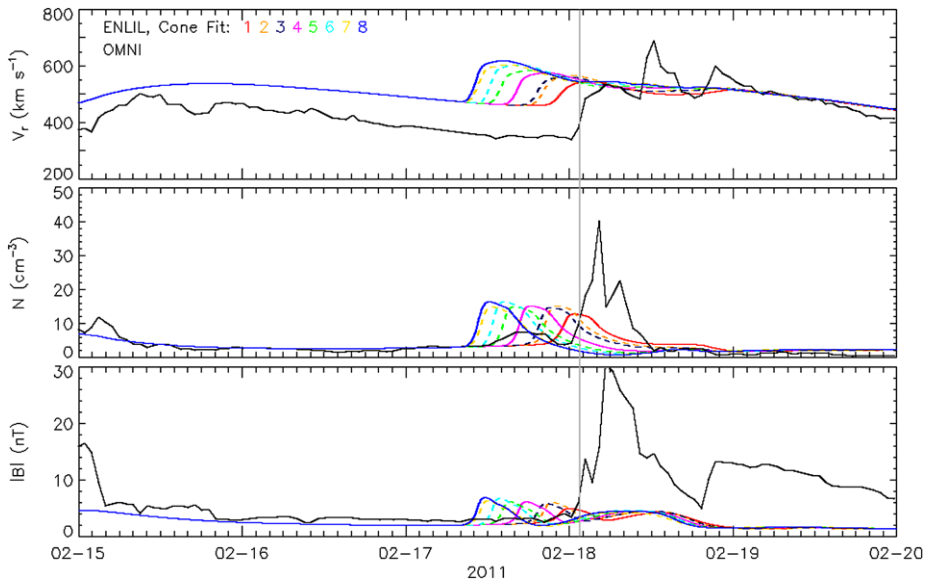


Figure 7 Time series of the near-ecliptic solar wind parameters at 1 AU for (top) radial speed, (middle) density, and (bottom) magnetic field magnitude. The colored lines are the simulation results from WSA-Enlil, where each color represents the simulation result for each cone fit from our ensemble for the 15 February 2011 CME. The *in situ* L1 observations from the OMNI data set are shown in solid black. The gray vertical line marks the approximate (observed) shock arrival time of the CME at Earth.

4. Sensitivity to the Solar Wind Background

To better understand the ensemble modeling results shown in Figure 7, we investigate whether the early predictions are solely due to the poor parameterization of the CME using the NOAA/SWPC cone tool by the authors, or a combination of that together with other factors (the WSA-Enlil modeling system, input photospheric map, *etc.*). We start by examining more closely the background (near-ecliptic) solar wind, especially during the several days leading up to the CME disturbance. Figure 7 (top panel) shows that prior to the CME arrival the modeled background solar wind speeds are $\sim 100 \text{ km s}^{-1}$ higher than the observed values. In contrast, the modeled background density values are comparable to the observations (Figure 7, middle panel). For the total magnetic field strength (Figure 7, bottom panel), the modeled values are underestimated in comparison to the observed values. The underestimation in the magnetic field is a well-known problem (see Owens *et al.*, 2007 and Lee *et al.*, 2009) and may be due to the magnetograms and how they are processed (see Owens *et al.*, 2007 and references therein).

Thus one possible explanation for the early arrival times in our ensemble set of predictions is due to the CME propagating into a solar wind stream that is faster than observed. As a quick test, we manually modified the values in the region of the WSA solar wind speed map (*e.g.*, Figure 6, top panel) where the cone CME parameters are prescribed in the Enlil simulation domain. This modified portion of the speed map is roughly centered around the ecliptic region (indicated by the + symbol in Figure 6, top panel) for the period. Using this modified speed map as the input driver for the Enlil solar wind model, we found that, by reducing the solar wind speeds in the region through which the cone CME propagates, both the near-ecliptic solar wind and the ensemble of CME arrival times were in significantly bet-

ter agreement with the observed values. The results from this *ad hoc* approach encouraged us to improve the background solar wind using a different and more rigorous method.

For this purpose, we utilized newly developed synoptic maps as input to WSA-Enlil. The commonly used Carrington rotation formatted synoptic maps, like the daily updated synoptic map from GONG used to generate the results shown in Figure 7, assume that the Sun rotates as a solid body with a rotational period of 27.2753 days. With such mixing of spatial measurements, the boundaries between the old and new observations can lead to large discontinuities that result in magnetic monopole signals. To avoid these discontinuities, new realizations for synoptic maps are starting to be produced that incorporate the known solar surface flows. These maps, generated by magnetic flux transport models, provide an instantaneous snapshot of the global photospheric magnetic field. The transport models evolve the global magnetic flux from previous measurements forward in time by applying rotational, meridional, and supergranular diffusive surface transport processes to predict the magnetic field in locations where direct measurements are not available (*e.g.*, Worden and Harvey, 2000; Schrijver and De Rosa, 2003; and references therein). The flux transport model used in this study is the ADAPT model (Arge *et al.*, 2010, 2011; Henney *et al.*, 2012), which employs a modified version of the Worden and Harvey flux transport model (Worden and Harvey, 2000). For this study, the ADAPT global photospheric maps were created using the line-of-sight magnetogram from the *Vector Spectromagnetograph* (Henney *et al.*, 2009).

Figure 5 (bottom panel) shows the ADAPT map of the photospheric fields. The map is presented so that it is aligned by the date labels on the NSO/GONG daily updated map (Figure 5, top panel). Overall, the gross magnetic field features on the ADAPT map are very similar to those on the GONG map, particularly in the low-to-mid-latitudinal regions (within $\pm 45^\circ$). However, in the polar regions (greater than $\pm 75^\circ$), where typically the measurements of the magnetic fields are of very poor quality or even lacking due to the line-of-sight issues (*e.g.*, the GONG map shown in Figure 5, top panel), the values are estimated with the flux transport of the ADAPT map (Figure 5, bottom panel).

Figure 6 (bottom panel) shows the resulting map of radial solar wind speeds at $21.5 R_\odot$ when the ADAPT map is used as input in the WSA corona model. Comparing the ADAPT-based radial speed map with the GONG-based one (top panel), the structure of the solar wind and the speeds are quite different. The differences arise because the magnetic fields in the GONG map are assembled in the traditional way and largely represent the time history of the central meridian over the period of Carrington rotation, whereas the ADAPT map represents the global magnetic field distribution at a single point in time as determined by the flux transport process in the model (see Arge *et al.*, 2011 for details). In particular, for this study, if we examine the ecliptic region (marked by the + symbol on 15 February 2011 in Figure 6, bottom panel) where the cone CME parameters are provided in the Enlil simulation domain, the ADAPT-based solar wind speeds are slower (more blue, $\sim 400 \text{ km s}^{-1}$) compared to the speeds in the same region on the GONG-based map (more green, $\sim 500 \text{ km s}^{-1}$).

Using the ADAPT map as input to drive the background solar wind, we generate a new set of WSA-Enlil-cone ensemble predictions. Figure 8 shows the new solar wind radial speeds, densities, and total magnetic field at 1 AU in the near-ecliptic plane. In Figure 8 (top panel), the modeled radial speeds (colored lines) using the ADAPT input map provide a much better match with the *in situ* values (solid black line), particularly during the days leading up to the arrival of the CME disturbance. By using a more accurate model background solar wind through which the cone CME propagates, we obtain a set of arrival time predictions that match the observations much better.

Table 2 lists the cone parameters that are used for the simulations (excluding the cone source locations, which are listed in Table 1), the predicted arrival times when the ADAPT

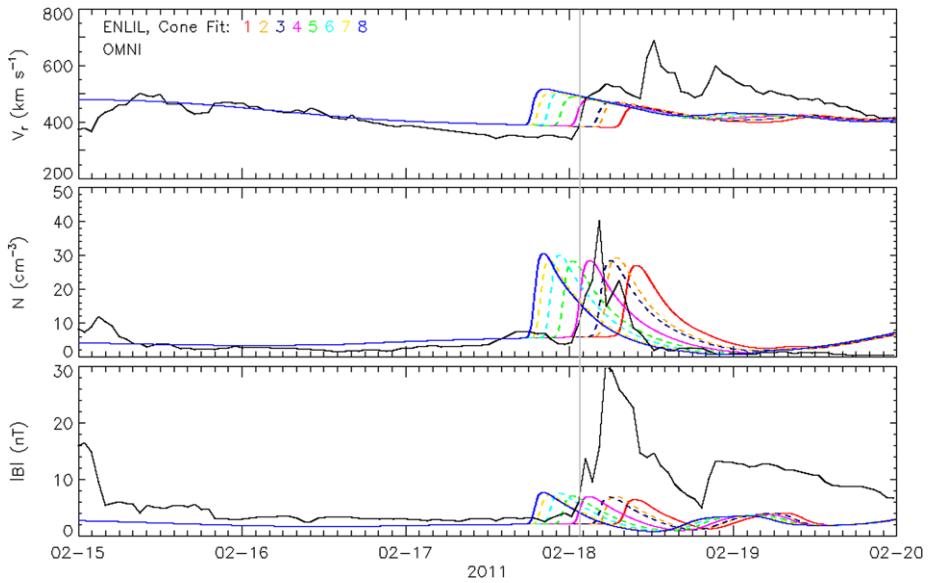


Figure 8 Same as for Figure 7, except here we used an ADAPT magnetic synoptic map as the inner boundary condition to drive the background solar wind.

Table 2 The cone fit parameters as listed in Table 1, except in the fourth column where we list the predicted arrival times, rounded to the next half hour, based on an ADAPT-driven background solar wind. The difference between the observed arrival time of $\sim 01:30$ UT on 18 February 2011 (as marked by the gray vertical line in Figure 8) and the predicted arrival time is listed in the fifth column ($\Delta t = t_{\text{observed}} - t_{\text{predicted}}$). In the last column, we also list for each fit Δt_{pred} , the difference between the ADAPT-based predicted arrival time *versus* the GONG-based arrival time ($t_{\text{ADAPT}} - t_{\text{GONG}}$).

Fit	Full width ($^{\circ}$)	V_R at $21.5 R_{\odot}$ (km s^{-1})	Predicted arrival time at 1 AU (UT)	Δt	Δt_{pred} ($t_{\text{ADAPT}} - t_{\text{GONG}}$)
1	68	558	08:00 18 Feb.	-6.5	-9.0
2	72	613	05:00 18 Feb.	-3.5	-9.0
3	68	622	04:00 18 Feb.	-2.5	-9.0
4	66	681	01:00 18 Feb.	+0.5	-9.0
5	62	727	23:00 17 Feb.	+2.5	-9.5
6	68	764	21:00 17 Feb.	+4.5	-9.0
7	62	806	19:30 17 Feb.	+6.0	-9.0
8	68	814	18:30 17 Feb.	+7.0	-8.5

map is used to drive the background solar wind, the difference between the ADAPT-based and the observed arrival times, and the difference in the predicted arrival times when the ADAPT synoptic map is used *versus* the GONG daily updated map ($\Delta t_{\text{pred}} = t_{\text{ADAPT}} - t_{\text{GONG}}$). In using the ADAPT map to obtain a more accurate background solar wind, the ensemble of shock arrival time predictions now bracket the observed arrival time (indicated by a vertical gray line). Based on our “average” cone fit, the predicted arrival time ($\sim 01:00$ UT on 18 February 2011) is off by ~ 0.5 hour compared to the actual arrival time of $\sim 01:30$ UT. If we refer to our earliest and latest prediction in our ensemble (blue and

red times series, respectively, in Figure 8), the effective error of our average prediction is approximately $+6.5/-7$ hours. Notice that the spread in the arrival times is similar to the spread when using the GONG daily updated map, indicating that the improvement to the background solar wind speed using ADAPT did not alter by much the spread in the CME arrival times.

With the improvement in the background solar wind, the modeled CME event densities are also in better agreement with the *in situ* values. In particular, the modeled CME densities for the “average” cone fit member in our ensemble (solid magenta line in Figure 8, middle panel) overlap the observed densities very well, where the peak amplitude of the modeled CME values is $\sim 30 \text{ cm}^{-3}$ compared to the observed value of $\sim 40 \text{ cm}^{-3}$. In comparison, when the GONG daily updated map was used as the input map for the WSA-Enlil-cone modeling system, the average peak amplitude of the modeled CME values was less than 20 cm^{-3} .

The difference in the peak amplitude values is most likely due to the inverse correlation between the solar wind speed and density that is imposed upon the Enlil results (recall that momentum flux is conserved in the model for the derivation of the mass density). In using ADAPT instead of GONG as input to WSA, the distribution of the radial solar wind speed changed at the Enlil inner boundary. Consequently, the new speed distribution modified the input stream structure so as to produce the higher densities at the solar wind stream structure that is propagating ahead of the cone CME.

Figures 9 and 10 present a more global view of the interplanetary solar wind structure during the CME event when the GONG daily updated or ADAPT synoptic map is used as the input driver, respectively. In both figures, the colors representing the solar wind density values and the color scales are the same. Three ecliptic-view time slices are shown in each figure to illustrate the injection of the cone CME into the inner boundary of the Enlil numerical domain (left panel), the cone CME propagating past the orbit of Venus at 0.7 AU (middle panel), and the cone CME reaching Earth at 1 AU (right panel). In both examples, the cone parameters from fit number 4 are used in the simulations (see Tables 1 and 2).

Figure 9 (left time panel) shows that when the GONG map is used to simulate the ambient solar wind, the cone CME is injected into a lower-density solar wind stream (blue) that is propagating ahead of it. Given the inverse correlation between the solar wind speed and density in Enlil, the cone CME propagates into a relatively faster solar wind stream (green values in the ecliptic region around 15 February in Figure 6, top panel). Consequently, the predicted CME arrival time to 1 AU is earlier than observed. However, when the ADAPT map is used the modeled CME is injected into a denser solar wind stream (aqua-green, in Figure 10, left panel) that is thus moving at relatively slower speeds (blue values in Figure 6, bottom panel). Figure 10 (right panel) shows that the CME arrives at Earth later by ~ 12 hours than the time obtained using the GONG input map (Figure 9, right panel). Comparing Figure 10 (right panel) with Figure 9 (right panel), note also that the ADAPT-driven background solar wind altered the evolution of the cone CME so that its eastern flank is extended further east of the Sun–Earth line than the cone CME that is propagating through the GONG-driven solar wind.

Overall, these results highlight an important cautionary point: the accuracy of the modeled arrival times not only depends on the input cone CME geometry, but also on the accuracy of the modeled background solar wind. In particular, it is important to obtain an accurate background solar wind during the several days leading up to the arrival of the CME disturbance.

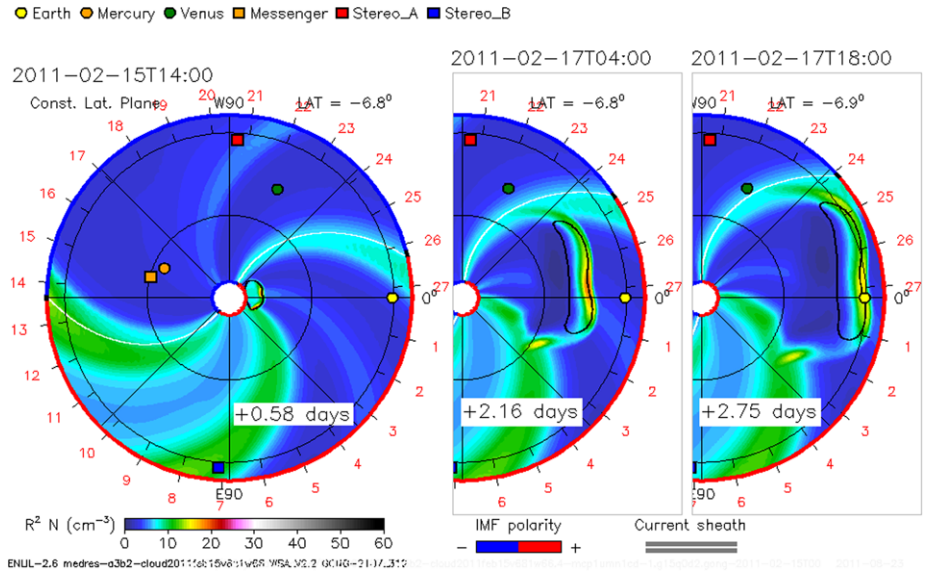


Figure 9 Ecliptic view of the evolution of the CME and the solar wind densities for fit number 4 (see Table 1 and Figure 7, middle panel), where a daily updated synoptic map from GONG is used to drive the background solar wind. The time steps shown from left to right are 0.58, 2.16, and 2.75 days after the start of the simulation time of 00:00 UT on 15 February 2011.

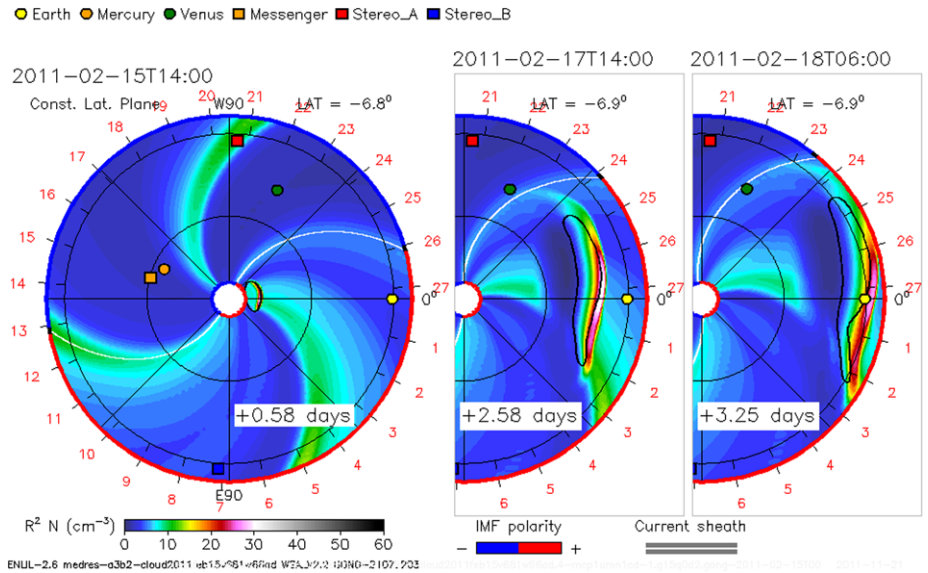


Figure 10 Similar to Figure 9, in which the same cone parameters are used, but here the background solar wind is driven with an ADAPT synoptic map (Figure 5, bottom panel). The time steps shown from left to right are 0.58, 2.58, and 3.25 days after start of the simulation time of 00:00 UT on 15 February 2011.

5. Sensitivity to the Initial Cone CME Parameters

In this section we discuss the sensitivity of the CME arrival time predictions to the small variations in the initial cone parameters. Because the ADAPT map did not alter much the spread in the arrival times when compared to the results using GONG, we focus specifically on the ensemble results that are generated when ADAPT was used to drive the background solar wind. Thus, we refer to the predicted arrival time values and their differences with the observed value listed in Table 2 (column 5).

We first examine a subset of ensemble predictions in which the same value for the cone angular width is used. Examining the list of values in Table 2, the value of 68° (full angular width) was used in fits 1, 3, 6, and 8. From these fits, the initial radial cone speeds (at $21.5 R_\odot$) of 558, 622, 764, and 814 km s^{-1} , respectively, were calculated using the cone tool. The predicted arrival times are shown in the fourth column of Table 2. For the slowest and fastest cases in this subset (fits 1 and 8, respectively), which are also the slowest and fastest cases in the entire ensemble, a difference of $\sim 250 \text{ km s}^{-1}$ in the initial CME speeds produced a spread of 13.5 hours.

The main source for the difference in the predicted arrival times for these two fits is primarily due to i) the time when the cone CME is injected into the Enlil simulation grid at $21.5 R_\odot$, which depends on ii) the value for the radial CME speed calculated from the NOAA/SWPC cone tool. For the first reason, a faster cone CME (*e.g.*, based on the parameters listed for fit number 8) is injected into the Enlil domain earlier than a slower cone CME (*e.g.*, based on the parameters listed for fit number 1). As a result, these cone CMEs are injected into slightly different parts of the input background solar wind (*e.g.*, from ADAPT) as it rotates westward at the Enlil inner boundary of $21.5 R_\odot$, and thus evolves differently in each case. For the second reason, recall from Section 2.2 that the values are calculated using the leading edge distance values together with the snapshot times of the LASCO CME images. In the cone tool, the size of the cone ellipse over the CME features is set by the leading edge distance values, which will vary depending on the user making the fit. For example, referring to Figure 4e, one user may choose to fit the ellipse as shown (in green) by tracking on a specific set of CME features. However, another user may track on slightly different CME features for the fitting and thereby encircle the ellipse around the CME more closely by setting a smaller value for the leading edge distance. Such variations in the fits will naturally occur due to the inherent subjectivity of the fitting process. With all factors being equal, for the subset of fits in which the same cone angular width is used (*e.g.*, fits 1, 3, 6, and 8), it follows that part of the spread in our ensemble of arrival time predictions is due to the variations in setting the leading edge distance values.

The fits are also compared when the cone angular widths are different but the initial radial cone speeds at $21.5 R_\odot$ are the same (to within 2 %). There are two such cases in our ensemble: i) fits 2 and 3 (or case 1) in which the cone angular widths are 72° and 68° and the initial speeds are 613 km s^{-1} and 622 km s^{-1} , and ii) fits 7 and 8 (or case 2) in which the cone angular widths are 62° and 68° and the initial speeds are 806 km s^{-1} and 814 km s^{-1} . For each case, the predicted arrival times differ by only about one hour. One might expect that, for a given halo CME line-of-sight observation, the use of a wider (narrower) angular width in the cone tool would produce an initial CME speed that is slower (faster). (Such a scenario was presented earlier in Section 2.1 and illustrated in Figure 2.) The situation is true for case 1 but not for case 2. Thus, although the cone angle used for the fits in each case is somewhat different (between 5 % to 10 %), the predicted arrival times only differed by a relatively small amount due to the similar values calculated for the initial cone speeds. As discussed previously, these initial speeds depend on the leading edge distance values used

for each “secondary” image throughout the fitting process. For the two cases just presented, in tuning the size of the cone ellipse the leading edge values were selected so that they offset the sensitivity of the initial cone speeds and the associated CME arrival times to the variations in the cone angular widths. Note that the one hour difference in the arrival times is in part due to the evolution and the propagation of the cone CME by the Enlil model.

Lastly, we note that the cone fits that used the narrowest and widest cone angles (62° by fits 5 and 7, and 72° by fit 2) did not produce the largest spread in our ensemble of arrival time predictions. Instead, the largest spread was produced by fits 1 and 8, in which the same cone angles were used (68°) but the variations in the leading edge distance values produced largely different radial CME speeds, as discussed earlier.

For this ensemble study, numerous cone fits were made for the 15 February 2011 CME event in order to assess the minimum number of fits required to obtain a representative spread in the CME arrival times when the WSA-Enlil-cone modeling system is used for forecasting CMEs. Our study is just one attempt at this assessment; thus additional ensemble studies are needed.

6. Conclusions

As we progress toward the next solar maximum, the WSA-Enlil-cone modeling system will be used for making routine space weather forecasts of geomagnetic storms. In particular, Earth-directed “halo” CMEs can trigger the most geoeffective storms, which impact and damage the technological systems in geospace. It is therefore important to understand the uncertainties in using the WSA-Enlil-cone modeling system for forecasting a CME arrival time.

In this study, we have presented an example of how one can assess the sensitivity of the WSA-Enlil-cone modeling results, such as CME arrival times, to small variations in the input cone CME properties. As an initial assessment of the model sensitivity, we selected the 15 February 2011 halo CME event for this study. We used a version of the geometric cone tool developed at NOAA/SWPC to create a single set of cone parameters, whereby the cone ellipse is fitted manually to a series of LASCO/C3 white light coronagraph images of the CME. In the cone tool, two free parameters, the leading edge distance of the CME front and the angular width, must be set by the user during the initial fittings. However, estimating these parameters using white light images taken along the Sun–Earth line is challenging due to unfavorable perspective effects. The 15 February 2011 CME event was specifically chosen to demonstrate the value of additional observations that were available from the highly advantageous locations of STEREO A and B, which observed the Earth-directed CME over the solar limb. In particular, the STEREO limb observations allowed the leading edge distance and angular width of the CME to be determined much more reliably.

Eight independent cone fits were made to the event in order to explore the sensitivity of the model-predicted CME arrival time to the realistic ranges of the angular width and the leading edge distance obtained through the use of the cone fitting tool. Guided by the STEREO limb observations of the CME, particularly the observation made at $\sim 04:08$ UT on 15 February 2011, each of the eight cone fits had values for the cone angular width and the leading edge distance that ranged from 62° to 72° and $10 R_\odot$ to $12.5 R_\odot$, respectively. The event was simulated for each cone fit using the WSA-Enlil model in medium (2°) grid resolution. The result was an ensemble set of runs with eight different CME arrival times having a spread of ~ 13 hours that overlapped and was nearly centered on the observed shock arrival time. One predicted CME arrival time differed from the observed value by

only about 0.5 hour. Based on our analysis for this single event study, both the variation in the leading edge distance and the angular width contributed to the total spread in the ensemble set of predictions, with the prime contributor being the leading edge distance.

During this ensemble study, we found that predicting shock arrival times accurately depends not only upon the input cone CME parameters but also on the reliable specification of the background solar wind, which in turn depends on the reliability of the input synoptic map of the photospheric magnetic field.

A major objective of this work is to better understand the sensitivity of the WSA-Enlil model to the input parameters (primarily based on the cone model fitting and the background solar wind specification) and how these parameters contribute to the overall model uncertainty and performance. Achieving this will result in a better understanding of the full predictive capability of the WSA-Enlil-cone modeling system. Because the ensemble spread and the factors contributing to it may be event dependent, a follow-on study will include several events and use a more systematic approach to estimate the leading edge distance and angular width of CMEs. For example, a large ensemble of fits to a given CME can be made in which the cone angular width is held fixed across a cone fit set wherein the leading edge distance value is made to vary systematically in increments of $0.25 R_{\odot}$. Our follow-on study will also assess the sensitivity of the predicted arrival times to the numerical grid resolution of the Enlil model. For space weather operations in particular, it will be important to know whether lower resolution simulations with a shorter turnaround time can be employed without greatly impacting the accuracy of the arrival time predictions.

Acknowledgements The authors thank the NASA Goddard Space Flight Center Space Physics Data Facility (SPDF) and National Space Science Data Center (NSSDC) for providing the OMNI data and OMNIWeb access, the National Solar Observatory *Global Oscillation Network Group* for providing access to their magnetogram and synoptic map data sets, and the agencies sponsoring these archives (NASA, NSF, USAF). The authors would like to acknowledge that SOHO is a project of international cooperation between the European Space Agency and NASA. In addition, the authors wish to express thanks to Drs. Joan Burkepile and Doug Biesecker for discussions regarding the complexities of characterizing halo CMEs from line-of-sight white light coronagraph images.

Christina O. Lee thanks the journal editors, special guest editors, and the referee for their assistance in evaluating and improving the content of this paper.

This research was performed while Christina O. Lee held a National Research Council Research Associateship Award at the Air Force Research Laboratory Space Vehicles Directorate in Kirtland Air Force Base, New Mexico and is supported by the Air Force Office of Scientific Research.

References

- Altschuler, M.D., Newkirk, G.: 1969, *Solar Phys.* **9**, 131–149.
- Arge, C.N., Pizzo, V.J.: 2000, *J. Geophys. Res.* **105**, 10465–10479.
- Arge, C.N., Odstrcil, D., Pizzo, V.J., Mayer, L.R.: 2003, In: *Solar Wind Ten, AIP Conf. Proc.* **679**, 190–193.
- Arge, C.N., Luhmann, J.G., Odstrcil, D., Schrijver, C.J., Li, Y.: 2004, *J. Atmos. Solar-Terr. Phys.* **66**, 1295–1309.
- Arge, C.N., Henney, C.J., Koller, J., Compeau, C.R., Young, S., MacKenzie, D., Fay, A., Harvey, J.W.: 2010, In: *Twelfth International Solar Wind Conference, AIP Conf. Proc.* **1216**, 343–346. doi:[10.1063/1.3395870](https://doi.org/10.1063/1.3395870).
- Arge, C.N., Henney, C.J., Koller, J., Toussaint, W.A., Harvey, J.W., Young, S.: 2011, In: Pogorelov, N.V., Audit, E., Zank, G.P. (eds.) *5th International Conference of Numerical Modeling of Space Plasma Flows: ASTRONUM-2010, ASP Conf. Series* **444**, 99–104.
- Brueckner, G.E., Howard, R.A., Koomen, M.J., Korendyke, C.M., Michels, D.J., Moses, J.D., Socker, D.G., Dere, K.P., Lamy, P.L., Llebaria, A., Bout, M.V., Schwenn, R., Simnett, G.M., Bedford, D.K., Eyles, C.J.: 1995, *Solar Phys.* **162**, 357–402.
- Burkepile, J.T., Hundhausen, A.J., Stanger, A.L., St. Cyr, O.C., Seiden, J.A.: 2004, *J. Geophys. Res.* **109**, A03103. doi:[10.1029/2003JA010149](https://doi.org/10.1029/2003JA010149).

- Byrne, J.P., Maloney, S.A., McAteer, R.T.J., Refojo, J.M., Gallagher, P.T.: 2010, *Nat. Commun.* **1**, 74. doi:[10.1038/ncomms1077](https://doi.org/10.1038/ncomms1077).
- Cohen, O., Sokolov, I.V., Roussev, I.I., Gombosi, T.: 2008, *J. Geophys. Res.* **113**, A03104. doi:[10.1029/2007JA012797](https://doi.org/10.1029/2007JA012797).
- Davis, C.J., de Koning, C.A., Davies, J.A., Biesecker, D., Millward, G., Dryer, M., Deehr, C., Webb, D.F., Schenk, K., Freeland, S.L., Mostl, C., Farrugia, C.J., Odstrcil, D.: 2011, *Space Weather* **9**, S01005. doi:[10.1029/2010SW000620](https://doi.org/10.1029/2010SW000620).
- Forsyth, R.J., Bothmer, V., Cid, C., Crooker, N.U., Horbury, T.S., Kecskemety, K., Blecker, B., Linker, J.A., Odstrcil, D., Reiner, M.J., Richardson, I.G., Rodriguez-Pacheco, J., Schmith, J.M., Wimmer-Schweingruber, R.F.: 2006, *Space Sci. Rev.* **123**, 383–416.
- Harvey, J.W., Hill, F., Hubbard, H.P., Kennedy, J.R., Leibacher, J.W., Pintar, J.A., Gilman, P.A., Noyes, R.W., Title, A.M., Toomre, J., Ulrich, R.K., Bhatnagar, A., Kennewell, J.A., Marquette, W., Patron, J., Saa, O., Yakasuwa, E.: 1996, *Science* **272**, 1284–1286.
- Henney, C.J., Keller, C.U., Harvey, J.W., Georgoulis, M.K., Hadder, N.L., Norton, A.A., Raouafi, N.E., Toussaint, R.M.: 2009, In: Berdyugina, S.V., Nagendra, K.N., Ramelli, R. (eds.) *Solar Polarization 5: In Honor of Jan Stenflo. ASP Conf. Series* **405**, 47–50.
- Henney, C.J., Toussaint, W.A., White, S.M., Arge, C.N.: 2012, *Space Weather* **10**, S02011. doi:[10.1029/2011SW000748](https://doi.org/10.1029/2011SW000748).
- Hundhausen, A.J., Burkepile, J.T., St. Cyr, O.C.: 1994, *J. Geophys. Res.* **99**, 6543–6552.
- Kaiser, M.: 2005, *Adv. Space Res.* **36**, 1483–1488.
- Lee, C.O., Luhmann, J.G., Odstrcil, D., MacNeice, P.J., de Pater, I., Riley, P., Arge, C.N.: 2009, *Solar Phys.* **254**, 155–183.
- Liu, Y., Thernisien, A., Luhmann, J.G., Vourlidis, A., Davies, J.A., Lin, R.P., Bale, S.D.: 2010, *Astrophys. J.* **722**, 1762–1777.
- Lugaz, N.: 2010, *Solar Phys.* **267**, 411–429.
- Mikić, Z., Linker, J.A.: 1995, In: Winterhalter, D., Gosling, J.T., Habbal, S.R., Kurth, W.S., Neugebauer, M. (eds.) *Solar Wind Eight, AIP Conf. Proc.* **382**, 104–107.
- Möstl, C., Rollett, T., Lugaz, N., Farrugia, C.J., Davies, J.A., Temmer, M., Veronig, A.M., Harrison, R.A., Crothers, S., Luhmann, J.G., Galvin, A.B., Zhang, T.L., Baumjohann, W., Biernat, H.K.: 2011, *Astrophys. J.* **741**, 34. doi:[10.1088/0004-637X/741/1/34](https://doi.org/10.1088/0004-637X/741/1/34).
- Odstrcil, D.: 2003, *Adv. Space Res.* **32**, 497–506.
- Odstrcil, D., Linker, J.A., Lionello, R., Mikic, Z., Riley, P., Pizzo, V.J., Luhmann, J.G.: 2002, *J. Geophys. Res.* **107**, 1493. doi:[10.1029/2002JA009334](https://doi.org/10.1029/2002JA009334).
- Owens, M.J., Spence, H.E., McGregor, S., Hughes, W.J., Quinn, J.M., Arge, C.N., Riley, P., Linker, J., Odstrcil, D.: 2007, *Space Weather* **6**, S08001. doi:[10.1029/2007SW000380](https://doi.org/10.1029/2007SW000380).
- Pizzo, V., Millward, G., Parsons, A., Biesecker, D., Hill, S., Odstrcil, D.: 2011, *Space Weather* **9**, S03004. doi:[10.1029/2011SW000663](https://doi.org/10.1029/2011SW000663).
- Riley, P., Linker, J.A., Mikic, Z.: 2001, *J. Geophys. Res.* **106**, 15889–15901.
- Schatten, K.H.: 1971, *Cosm. Electrodyn.* **2**, 232–245.
- Schatten, K.H., Wilcox, J.M., Ness, N.F.: 1969, *Solar Phys.* **6**, 442–455.
- Schrijver, C.J., De Rosa, M.L.: 2003, *Solar Phys.* **212**, 165–200.
- Wang, Y.M., Sheeley, N.R. Jr.: 1992, *Astrophys. J.* **392**, 310–319.
- Wang, Y.M., Sheeley, N.R. Jr.: 1995, *Astrophys. J.* **447**, L143–L146.
- Webb, D.F., Allen, J.: 2004, *Space Weather* **2**, S03008. doi:[10.1029/2994SW000075](https://doi.org/10.1029/2994SW000075).
- Webb, D.F., Kahler, S.W., McIntosh, P.S., Klimchuck, J.A.: 1997, *J. Geophys. Res.* **102**, 24161–24174.
- Worden, J., Harvey, J.: 2000, *Solar Phys.* **195**, 247–268.
- Xie, H., Ofman, L., Lawrence, G.: 2004, *J. Geophys. Res.* **109**, A03019. doi:[10.1029/2003JA010226](https://doi.org/10.1029/2003JA010226).
- Zhao, X.P., Plunkett, S.P., Liu, W.: 2002, *J. Geophys. Res.* **107**, 1223. doi:[10.1029/2001JA009143](https://doi.org/10.1029/2001JA009143), SSH 13-1.